Materials Horizons

ROYAL SOCIETY OF CHEMISTRY

COMMUNICATION

View Article Online
View Journal | View Issue

Cite this: *Mater. Horiz.*, 2026, 13, 326

Received 24th August 2025,
Accepted 18th September 2025

DOI: 10.1039/d5mh01620g

rsc.li/materials-horizons

Cobalt oxide–supported iridium oxide nanoparticles with strong metal oxide–support interaction for efficient acidic oxygen evolution reaction

Hao Deng,[a] Chung-Li Dong,[b] Ta Thi Thuy Nga,[b] Miao Wang,[a] Yiduo Wang,[a] Yiqing Wang[a] and Shaohua Shen *[a]

Understanding and regulating the deprotonation process in an acidic oxygen evolution reaction (OER) is highly desirable for a proton exchange membrane water electrolyzer (PEMWE). Herein, ultrasmall IrO_2 nanoparticles were firmly anchored on an acid-resistant Co_3O_4 support (IrO_2/Co_3O_4) through galvanic replacement, with strong metal oxide–support interaction (SMOSI) induced and responsible for the accelerated deprotonation process during OER. For IrO_2/Co_3O_4, a low overpotential of 256 mV at 10 mA cm^{-2} could be achieved for an acidic OER, with sustained operation exceeding 1000 h. More importantly, a PEMWE assembled with IrO_2/Co_3O_4 as the anode could survive 120 h and 40 h of operation at industrial-level current densities of 0.5 and 1 A cm^{-2}, with cell voltages of 1.64 and 1.77 V, respectively. Experimental results and theoretical calculations together demonstrate that the SMOSI induced by the lattice-mismatched interfaces in IrO_2/Co_3O_4 could increase the p-band center of O_{bri} (bridging oxygen) sites in the Ir–O_{bri} bonds. Such an enhanced p-band center would strengthen the proton acceptance of O_{bri} sites, facilitating the deprotonation process, and thus improving OER activity and stability. This work presents an alternative approach for the regulation of the deprotonation process *via* SMOSI and the design of an inexpensive and efficient electrocatalyst towards an industrial-level PEMWE.

New concepts

Accelerating the deprotonation process during an acidic oxygen evolution reaction (OER) is an effective strategy to break the scaling relationship in the conventional adsorbate evolution mechanism (AEM). In this work, the concept of strong metal oxide–support interaction (SMOSI) has been demonstrated to regulate the deprotonation process in acidic OER, to improve OER activity and reduce the mass loading of noble Ir. As evidenced by experimental results and theoretical calculations, SMOSI could be induced by anchoring ultrasmall IrO_2 nanoparticles on a Co_3O_4 support (IrO_2/Co_3O_4) through galvanic replacement. Such SMOSI strengthens the proton acceptance of bridging oxygen (O_{bri}) sites in the Ir–O_{bri} bonds, thereby accelerating the deprotonation process in OER. Consequently, a deprotonation-assisted adsorbate evolution mechanism (DAEM) could be reasonably proposed to elucidate the excellent performance for acidic OER over IrO_2/Co_3O_4, by breaking the scaling relationship in conventional AEM. This study demonstrates a promising approach to regulating the deprotonation process on O_{bri} sites *via* SMOSI for efficient and stable acidic OER, and also inspires the design of applicable and low-noble-metal electrocatalysts for industrial-level PEMWE.

1. Introduction

Hydrogen, with its high energy density, is widely recognized as a promising candidate for next-generation clean energy, when produced *via* water electrolysis powered by green electricity generated from renewable energy.[1–4] Among various water electrolysis technologies, the proton exchange membrane water electrolyzer (PEMWE) has attracted worldwide interest due to its high current density (>1 A cm^{-2}), high hydrogen purity (>99.99%), and fast response (<5 s) for intermittent renewable electricity.[5–7] However, the industrial application of PEMWE is substantially impeded by the absence of affordable and highly efficient electrocatalysts at the anode for an acidic oxygen evolution reaction (OER).[8–10] In general, Ir and its derived oxides have been exclusively considered to be the only viable electrocatalysts to meet the requirements of high activity for OER and excellent stability under harsh acidic conditions in a PEMWE, while the scarcity of noble Ir has drastically limited its large-scale application.[11–13] Thus, significant efforts have focused on lowering the mass loading of Ir at the anode while enhancing electrocatalytic OER activity for practical PEMWE applications.[14,15]

Dispersing Ir-based active species on high-surface-area supports has been considered an effective strategy towards

[a] *International Research Center for Renewable Energy, State Key Laboratory of Multiphase Flow in Power Engineering, Xi'an Jiaotong University, Xi'an 710049, China. E-mail: shshen_xjtu@mail.xjtu.edu.cn*
[b] *Department of Physics, Tamkang University, Tamsui 25137, Taiwan*

improved OER performance with optimized utilization of noble Ir for electrocatalysis. These reported support materials, *e.g.*, MnO_2, Nb_2O_{5-x}, TaO_x, TiO_2, and Co_3O_4,[16–21] are expected to exhibit high resistance to acid corrosion and oxidative decomposition to ensure stable dispersion of Ir-based active species. Among them, Co_3O_4 has been recognized as an effective support material for loading Ir-based active species,[22–26] enhancing the electrocatalytic activity and stability of Ir active sites in acidic OER. For example, by incorporating Ir single atoms on the Co_3O_4 support, the obtained Ir–Co_3O_4 electrocatalyst reached a current density of 10 mA cm^{-2} for acidic OER at a small overpotential of 236 mV, with an Ir loading of only 1.05 at%.[22] However, due to weak interaction with the Co_3O_4 support, the Ir single atoms in this electrocatalyst tend to dissolve during the OER process, resulting in limited stability at industrial-level current densities that requires further enhancement. Besides, the OER pathway determined by the interactions between the Ir-based active species and the Co_3O_4 support remains unclear and requires further exploration. The activity and stability for OER over Ir-based active species are believed to depend on the OER pathway. It was revealed that OER taking place at rutile IrO_2 should follow the conventional adsorbate evolution mechanism (AEM), which is limited by the scaling relationship between the adsorption energies of OH* and OOH* intermediates, with a theoretical minimum overpotential of *ca.* 370 ± 100 mV.[27–29] By manipulating the OER intermediates, this limitation in AEM can be overcome *via* the lattice-oxygen-mediated mechanism (LOM), in which activated lattice oxygen participates in the O–O coupling process to improve OER.[30–32] However, the oxygen defects generated *via* LOM would cause the rapid degradation and deactivation of electrocatalysts under acidic OER conditions.[33] Recently, an accelerated deprotonation process during OER by incorporating dopants into IrO_2 or RuO_2 has been proposed and confirmed to break the scaling relationship without sacrificing OER stability.[34–38] For instance, by introducing Sb dopants into the RuO_2 lattice to construct highly asymmetric Ru–O–Sb units, the deprotonation process of oxygen-containing intermediates taking place at bridging oxygen (O_{bri}) sites was significantly promoted for the obtained $Ru_{0.8}Sb_{0.2}O_2$, which required a low overpotential of 160 mV at 10 mA cm^{-2} and maintained a good stability of 1100 h for acidic OER.[37] With such a deprotonation process regarded as an additional chemical step in AEM, the theoretical overpotential was significantly decreased to 0.35 V, compared to that of conventional AEM (0.69 V).[37] However, the deprotonation process regulated by incorporating dopants relies heavily on noble metals as the main components, which inevitably affords a remarkable increase in the cost of electrocatalysts. Anticipating a significant improvement in both the activity and stability of electrocatalysts for acidic OER, it would be encouraging but challenging to accelerate the deprotonation process in the OER pathway, with Ir content reduced by introducing a Co_3O_4 support to promise a high-performance and cost-effective OER. Considering the strong metal oxide–support interaction (SMOSI) between the Ir-based active species and the Co_3O_4 support,[39,40] which may determine the OER pathway and thus acidic OER activity, it is anticipated that elucidating the SMOSI-regulated deprotonation mechanism can guide the rational design of Ir-based electrocatalysts for practical industrial-scale PEMWE applications.

Motivated by the above insights, herein, ultrasmall IrO_2 nanoparticles were firmly anchored on the acid-resistant Co_3O_4 support (IrO_2/Co_3O_4) through galvanic replacement, with the induced SMOSI responsible for the accelerated deprotonation process for acidic OER. In comparison to commercial IrO_2, the obtained IrO_2/Co_3O_4 exhibits an excellent acidic OER performance, with a significantly lowered overpotential of 256 mV at a current density of 10 mA cm^{-2} for sustained operation exceeding 1000 h. Impressively, a PEMWE assembled with IrO_2/Co_3O_4 as the anode and Pt/C as the cathode could be operated stably for at least 120 and 40 h at industrial-level current densities of 0.5 and 1 A cm^{-2}, with cell voltages of 1.64 and 1.77 V, respectively. As evidenced by experimental results and theoretical calculations, the SMOSI generated at the lattice-mismatched interfaces of the anchored IrO_2 nanoparticles and the Co_3O_4 support could increase the p-band centers of O_{bri} sites towards the strengthened acceptance of protons, and thus accelerate the deprotonation process during acidic OER. These findings should be able to guide the steering of proton transfer behavior and thus the deprotonation process for efficient acidic OER, while also proposing an alternative strategy for the design of inexpensive and efficient electrocatalysts *via* SMOSI for an industrial-level PEMWE.

2. Results and discussion

Herein, to anchor IrO_2 nanoparticles on Co_3O_4 as support (IrO_2/Co_3O_4) with strong metal oxide–support interaction (SMOSI) induced at interfaces, metallic Co was first electrodeposited on titanium felt (TF), followed by the galvanic replacement of Ir species (Fig. 1a).[41] The spontaneous galvanic replacement occurring between the metallic Co and the Ir^{3+} ions in precursor solution ($2Ir^{3+} + 3Co \rightarrow 2Ir + 3Co^{2+}$) would then result in the formation of Ir nanoparticles well anchored on the surface of metallic Co (Ir/Co), due to the favorable thermodynamic process. Through the subsequent calcination and acid leaching processes, the well-optimized IrO_2/Co_3O_4 electrode with IrO_2 nanoparticles supported on Co_3O_4 could then be obtained from Ir/Co for an efficient oxygen evolution reaction (OER) (Fig. S1), with a low mass loading of Ir determined to be *ca.* 0.36 mg_{Ir} cm^{-2} by inductively coupled plasma-mass spectrometry (ICP-MS, Table S1). As shown in Fig. 1b, four Raman bands are clearly positioned at *ca.* 480, 522, 620, and 690 cm^{-1}, corresponding to the E_g bending, F^2_{2g} bending, F_{2g} stretching, and A_{1g} stretching vibration in the Co_3O_4 phases,[42] respectively. Raman bands related to IrO_2 could hardly be observed, demonstrating that the IrO_2 phases exist in a small proportion or with a particle size below the Raman detection limit, with Co_3O_4 phases dominating in IrO_2/Co_3O_4. It should be carefully noted that the Raman signal peaking at *ca.* 690 cm^{-1} exhibits a slight red-shift for IrO_2/Co_3O_4 compared to Co_3O_4, implying lattice

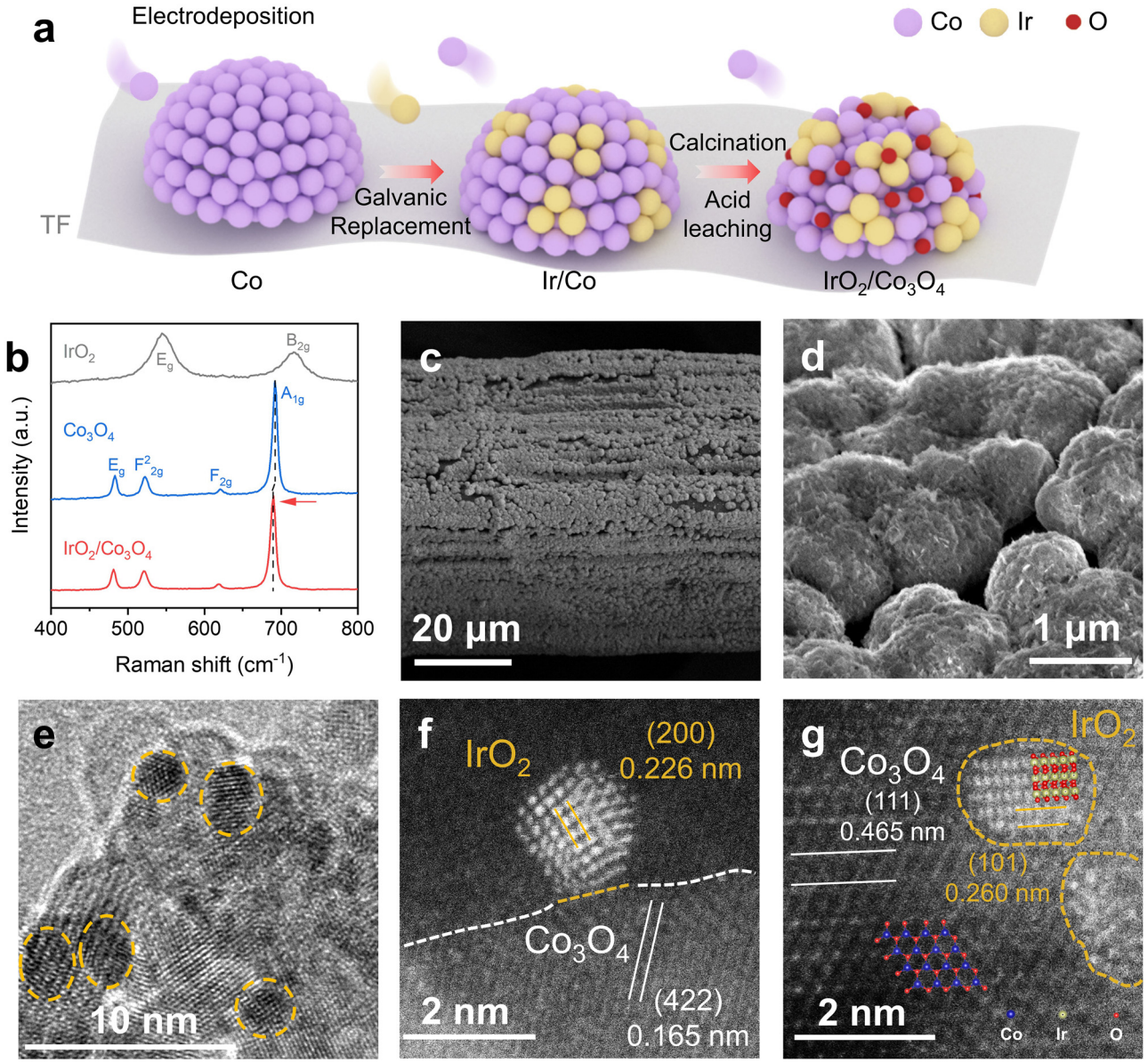

Fig. 1 (a) Schematic process for the synthesis of an IrO_2/Co_3O_4 electrode with IrO_2 nanoparticles anchored on a Co_3O_4 support. (b) Raman spectra of commercial IrO_2, Co_3O_4 and IrO_2/Co_3O_4. (c) and (d) SEM images, (e) HRTEM images and (f) and (g) AC HAADF-STEM images of IrO_2/Co_3O_4.

strain to the Co_3O_4 phases anchored with IrO_2 nanoparticles, as also confirmed by powder X-ray diffraction (XRD) patterns (Fig. S2). Scanning electron microscopy (SEM) images reveal a particulate structure with a coarse surface for both Co_3O_4 (Fig. S3) and IrO_2/Co_3O_4 (Fig. 1c and d) deposited on TF, which should be beneficial for the exposure of abundant active sites and thus promote mass transfer. As identified by high-resolution transmission electron microscopy (HRTEM) and aberration-corrected high-angle annular dark-field scanning transmission electron microscopy (AC HAADF-STEM) images, ultrasmall IrO_2 nanoparticles of 2–4 nm in average size (Fig. 1e) are firmly anchored on the surface of the Co_3O_4 support, given lattice fringes with *d*-spacings of 0.165 and 0.226 nm attributed to the (422) plane of Co_3O_4 and the (200) plane of IrO_2 (Fig. 1f), respectively. Further analysis on the top-view AC HAADF-STEM image (Fig. 1g) reveals a significant lattice mismatch at the interface between the (111) plane of Co_3O_4 and the (101) plane of IrO_2, with the lattice spacings at ordered atomic arrangements determined to be 0.465 and 0.260 nm, respectively.

Due to the much smaller lattice spacing of the IrO_2 (101) plane than the Co_3O_4 (111) plane, the Ir–O bonds of IrO_2 nanoparticles should be elongated by tensile strain, while the Co_3O_4 support undergoes compressive strain at the interface. Such interfacial lattice mismatch would lead to structural distortion of the IrO_2 nanoparticles and the Co_3O_4 support, referring to SMOSI, and thus inducing compressive strain in the Co_3O_4 support.[43–45] Given the homogeneous distribution of Ir, Co and O in the IrO_2/Co_3O_4 electrode (Fig. S4), abundant

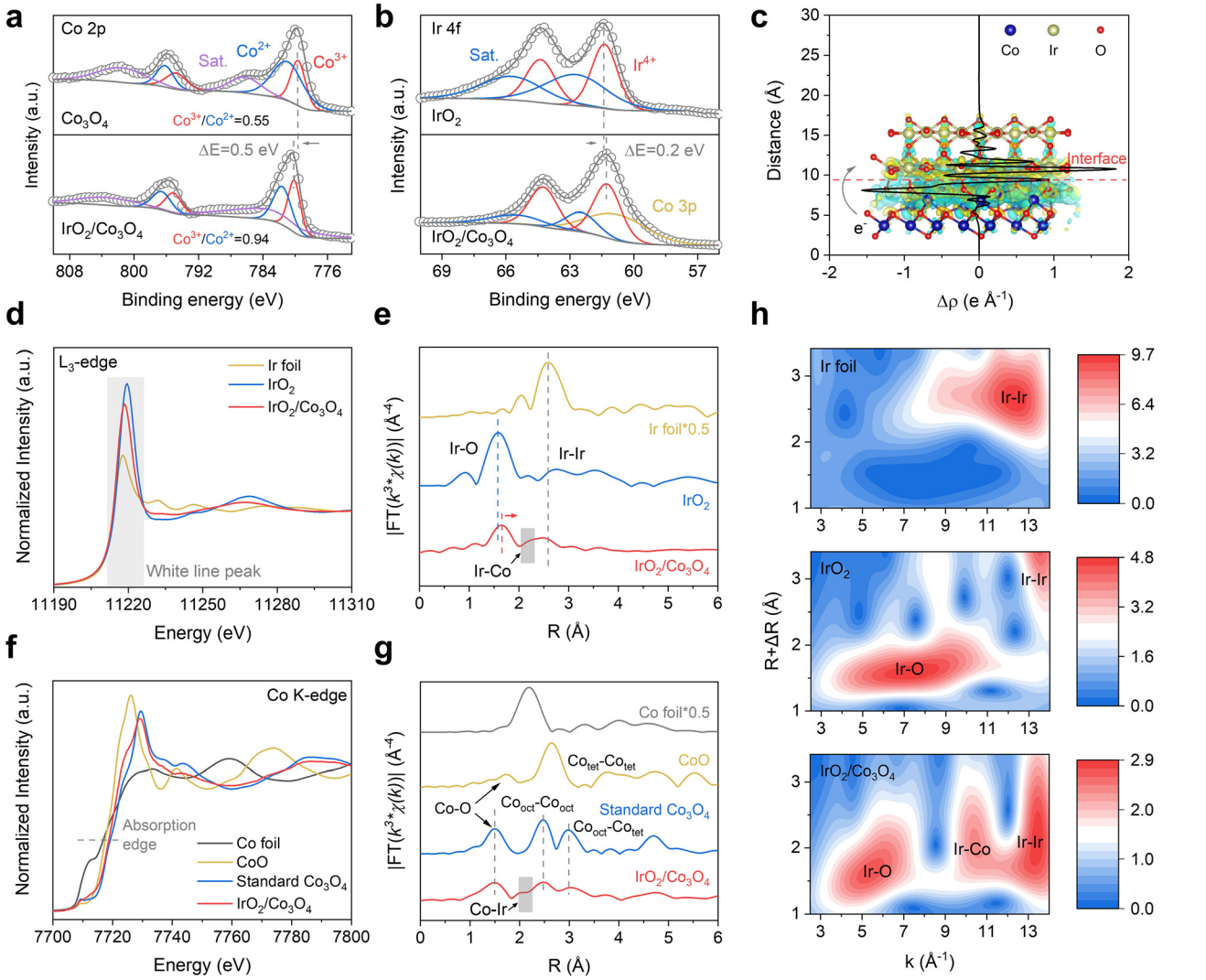

Fig. 2 (a) Co 2p XPS spectra of Co_3O_4 and IrO_2/Co_3O_4, (b) Ir 4f XPS spectra of IrO_2 and IrO_2/Co_3O_4. (c) Differential charge density patterns and planar-average charge density plots of IrO_2/Co_3O_4. The yellow and cyan contours represent electron accumulation and depletion regions, respectively. (d) Normalized XANES and (e) FT-EXAFS spectra of Ir foil, IrO_2 and IrO_2/Co_3O_4 collected at the Ir L_3-edge. (f) Normalized XANES and (g) FT-EXAFS spectra of Co foil, CoO, standard Co_3O_4 and IrO_2/Co_3O_4 collected at the Co K-edge. (h) Wavelet-transformed EXAFS spectra of Ir foil, IrO_2 and IrO_2/Co_3O_4 collected at the Ir L_3-edge.

lattice-mismatched IrO_2/Co_3O_4 heterostructures should be created, with IrO_2 nanoparticles firmly anchored at the surface of the Co_3O_4 support through galvanic replacement.

The electronic structures and chemical compositions of the IrO_2/Co_3O_4 electrode were then investigated by X-ray photoelectron spectroscopy (XPS). It is distinctly observed that with IrO_2 nanoparticles anchored on Co_3O_4, the Co^{3+} $2p_{3/2}$ signal located at *ca.* 779.6 eV is shifted to higher binding energy by 0.5 eV,[46] with the Co^{3+}/Co^{2+} ratio much increased from 0.55 for Co_3O_4 to 0.94 for IrO_2/Co_3O_4 (Fig. 2a). Such an XPS peak shift and increased Co^{3+}/Co^{2+} ratio suggest that the Co atoms should serve as electron donors, when IrO_2 nanoparticles interface with the Co_3O_4 support in the IrO_2/Co_3O_4 electrode. Moreover, the Ir^{4+} $4f_{7/2}$ signal observed at *ca.* 61.3 eV is shifted to a lower binding energy by 0.2 eV for IrO_2/Co_3O_4 compared to IrO_2 (Fig. 2b).[47,48] This negative shift in binding energy indicates that the Ir atoms in the IrO_2 phases accept electrons from the Co_3O_4 support, again suggesting charge redistribution at the interfaces in IrO_2/Co_3O_4 caused by interfacial lattice mismatch (Fig. 1f and g), agreeing well with the Co 2p XPS analysis (Fig. 2a). The atomic ratio of Co:Ir was determined to be 2.8 : 1 for IrO_2/Co_3O_4 by XPS analysis (Table S2), which, together with the absence of an IrO_2 signal in Raman spectra (Fig. 1b), indicates the high dispersion of IrO_2 nanoparticles at the surface of the Co_3O_4 substrate. Density functional theory (DFT) calculations were performed to confirm the above-discovered charge transfer behavior in the lattice-mismatched structure model of IrO_2/Co_3O_4 (Fig. S5).

It is observed that charge accumulation occurs in the IrO_2, while the charge depletion occurs in the Co_3O_4 phase (Fig. 2c), providing evidence of charge redistribution at the IrO_2/Co_3O_4 interfaces. This evolution in electronic structure in the

obtained IrO_2/Co_3O_4 electrode confirms SMOSI as induced by the lattice-mismatched interfaces between the anchored IrO_2 nanoparticles and the Co_3O_4 support.

To further distinguish the atomic coordination structure of IrO_2 nanoparticles anchored on the Co_3O_4 support, X-ray absorption spectroscopy (XAS) measurements were carried out for the IrO_2/Co_3O_4 electrode. The normalized X-ray absorption near-edge structure (XANES) spectra collected at the Ir L_3-edge show that the white-line peak at 11216–11219 eV (Fig. 2d), related to the electronic transition from occupied Ir 2p to empty Ir 5d orbitals,[49] is slightly lower for IrO_2/Co_3O_4 than for IrO_2, which indicates the higher electron density at the Ir 5d orbitals in IrO_2/Co_3O_4, attributed to electrons transferred from Co_3O_4 to IrO_2 (Fig. 2b). By determining the white-line position, the average oxidation state of Ir could then be calculated as +3.60 in IrO_2/Co_3O_4 with Ir foil and IrO_2 as references (Fig. S6). The coordination structures were further investigated from the Fourier-transform (FT) extended X-ray absorption fine structure (EXAFS) spectra (Fig. 2e). The peak located at *ca.* 1.56 Å, assigned to the Ir–O scattering path, is slightly shifted to higher R space for IrO_2/Co_3O_4 compared to IrO_2. This slight shift suggests elongated Ir–O bonds in IrO_2/Co_3O_4, as supported by the well-fitted EXAFS spectra, with the Ir–O bond lengths determined to be 1.97 Å in IrO_2 and 2.00 Å in IrO_2/Co_3O_4 (Fig. S7 and Table S3). These elongated Ir–O bonds in IrO_2/Co_3O_4 should be ascribed to the weakened Ir–O bond strength caused by the increased electron density at Ir atoms *via* SMOSI (Fig. 2d). Moreover, except for the peak located at *ca.* 2.48 Å for the Ir–Ir scattering path, another weak shoulder peak could be noted at *ca.* 2.10 Å in the Ir L_3-edge EXAFS spectra of IrO_2/Co_3O_4 (Fig. 2e). Such a weak shoulder peak belongs to the Ir–Co scattering path,[50,51] resulting from the abundant interfaces created between the anchored IrO_2 nanoparticles and the Co_3O_4 support. As for normalized XANES spectra collected at the Co K-edge, the oxidation state of Co could be evaluated from the absorption edge, which is determined by the position of half height in the normalized XANES spectra.[52] Interestingly, the absorption edge displays a slight shift to lower energy for IrO_2/Co_3O_4 compared to the standard Co_3O_4 (Fig. 2f), implying the relatively lower Co oxidation state in IrO_2/Co_3O_4. The EXAFS spectra collected at the Co K-edge were then studied to analyze the coordination structure of Co atoms in IrO_2/Co_3O_4 (Fig. 2g), with peaks clearly observed at *ca.* 1.5, 2.5 and 3.0 Å, corresponding to the Co–O, Co_{oct}–Co_{oct} (oct: octahedral sites) and Co_{oct}–Co_{tet} (tet: tetrahedral sites) scattering paths, respectively. By further fitting the EXAFS spectra (Fig. S8), one could note that the coordination number of Co–O is lower for IrO_2/Co_3O_4 than for standard Co_3O_4 (Table S3), which should be related to the formation of oxygen vacancies and thus, the decreased oxidation state of Co in IrO_2/Co_3O_4 (Fig. 2f). In addition, the fitted bond lengths of Co–O, Co_{oct}–Co_{oct} and Co_{oct}–Co_{tet} are smaller in IrO_2/Co_3O_4 than in Co_3O_4 (Table S3), which are again evidence for compressive strain in the Co_3O_4 support, well matching the analysis of the Raman spectra (Fig. 1b) and XRD patterns (Fig. S2b). One weak shoulder peak assigned to the Co–Ir scattering path could also be observed at *ca.* 2.10 Å in the Co K-edge EXAFS spectra (Fig. 2g), as previously discovered in the Ir L_3-edge EXAFS spectra (Fig. 2e). By fitting the EXAFS spectra, the Ir–Co bond lengths are determined to be 2.66 Å in IrO_2/Co_3O_4 (Table S3), smaller than the Co_{oct}–Co_{oct} bond lengths of 2.87 Å in standard Co_3O_4 and the Ir–Ir bond lengths of 3.10 Å in IrO_2 (Table S3), as also observed for the Ir–Co bonds in the structural model of IrO_2/Co_3O_4 (Fig. S5). These reduced Ir–Co bond lengths should be attributed to structural distortion at the interface between the IrO_2 nanoparticles and the Co_3O_4 support, as induced by the interfacial lattice mismatch. To distinguish the Ir–Co scattering path, wavelet-transform analysis was further performed in the Ir L_3-edge EXAFS spectra. With Ir foil and IrO_2 as references (Fig. 2h, upper and middle), the intensity maxima positioned at $k \approx 6$–8.5 Å^{-1} and 11.5–14 Å^{-1} should be attributed to the Ir–O and Ir–Ir scattering paths, respectively. Notably, an additional intensity maximum could be detected at $k \approx 10$–11 Å^{-1} for IrO_2/Co_3O_4 (Fig. 2h, bottom), which should be ascribed to the Ir atom bonded with the Co atom, confirming the presence of the Ir–Co scattering path.[24] The above spectral analyses are evidence that the IrO_2 nanoparticles anchored on the Co_3O_4 support would generate abundant Ir–Co bonds at the lattice-mismatched interfaces of IrO_2/Co_3O_4, with the induced SMOSI elongating the Ir–O bonds, which is believed to regulate OER intermediate behavior for improved OER performance, as revealed in the following discussions.

The electrocatalytic activity for acidic OER over the obtained IrO_2/Co_3O_4 electrode was evaluated in 0.5 M H_2SO_4 electrolyte in a three-electrode system, with a graphite rod and a calibrated Hg/Hg_2SO_4 electrode used as the counter and reference electrodes, respectively. In comparison to Co_3O_4, the IrO_2/Co_3O_4 electrode exhibits a great increase in OER performance, with a small overpotential of only 256 mV required to achieve a current density of 10 mA cm^{-2}, much lower than that of commercial IrO_2 (340 mV) as the benchmark OER electrocatalyst (Fig. 3a). Depending on the increasing applied potentials, the IrO_2/Co_3O_4 electrode could reach current densities of 100 and 500 mA cm^{-2} for OER at overpotentials of 308 and 373 mV, respectively. By further noting the great decrease in OER activity observed for the IrO_2 nanoparticles with Co_3O_4 support etched by acid (Fig. S9), SMOSI between the anchored IrO_2 nanoparticles and the Co_3O_4 support should contribute significantly to the enhancement in the intrinsic OER activity of IrO_2 for the IrO_2/Co_3O_4 electrode. To confirm the above deduction, the mass activity is calculated to have increased by 133 times, from 1.5 A g_{Ir}^{-1} for commercial IrO_2 to 200 A g_{Ir}^{-1} for the IrO_2/Co_3O_4 electrode at 1.53 V *vs.* RHE (Fig. 3b), which outperforms most reported Ir-based electrocatalysts for acidic OER (Table S4). Benefiting from SMOSI, the obtained IrO_2/Co_3O_4 electrode displays significantly improved OER kinetics, evidenced by a much decreased Tafel slope (54 mV dec^{-1}) compared to commercial IrO_2 (73 mV dec^{-1}) (Fig. 3c). Such kinetic improvement could be solidly supported by analysis of the electrochemical impedance spectroscopy (EIS), with charge transfer resistance (R_{ct}) decreasing from 3.79 Ω cm^2 for commercial IrO_2 to 0.42 Ω cm^2 for IrO_2/Co_3O_4 (Fig. 3d and Fig. S10).

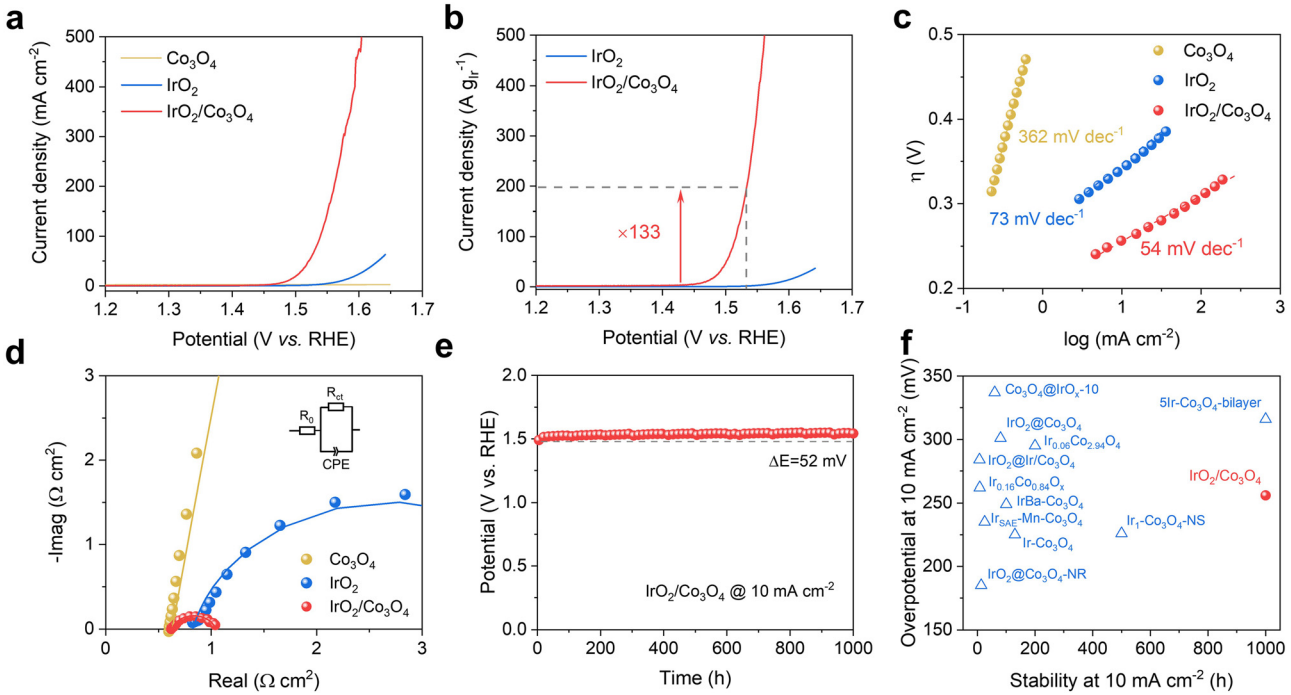

Fig. 3 (a) Linear sweep voltammetry (LSV) plots of commercial IrO_2, Co_3O_4 and IrO_2/Co_3O_4. (b) Mass activities of Ir for commercial IrO_2 and IrO_2/Co_3O_4. (c) Tafel and (d) EIS plots of commercial IrO_2, Co_3O_4 and IrO_2/Co_3O_4. (e) Chronopotentiometric plots of IrO_2/Co_3O_4 for stability testing. (f) Activity and stability of IrO_2/Co_3O_4 and the other reported electrocatalysts of Ir species dispersed on Co-based oxides.

This reduction is attributed to the significantly increased electrochemically active surface areas (ECSAs) from 284 cm^2 for commercial IrO_2 to 1946 cm^2 for IrO_2/Co_3O_4, as determined from current–scan rate plots (Fig. S11). Notably, chronopotentiometry measurements reveal negligible change in the overpotentials for OER at current densities of 10 and 200 mA cm^{-2} over 1000 (Fig. 3e) and 250 h operations (Fig. S12), respectively, indicating the excellent stability of the IrO_2/Co_3O_4 electrode for OER under acidic conditions. Scanning electron microscopy with energy-dispersive X-ray spectroscopy (SEM-EDS) and XPS analysis were then performed to assess the elemental dissolution of the IrO_2/Co_3O_4 electrode during OER. After OER for 24 h at a current density of 200 mA cm^{-2}, the atomic ratio of Co : Ir in the IrO_2/Co_3O_4 electrode was determined to have decreased significantly from 1.9 : 1 to 0.9 : 1 by EDS (Fig. S13) and from 2.8 : 1 to 1.2 : 1 by XPS (Table S2). Such a decrease in the Co : Ir ratio suggests that the Co_3O_4 support would be partially dissolved into the 0.5 M H_2SO_4 electrolyte under OER conditions, with IrO_2 phases dominating at the surface of the IrO_2/Co_3O_4 electrode during OER. The elemental dissolution of Co and Ir in the electrolyte during OER was further identified by ICP-MS analysis. It is revealed that Co species would be gradually dissolved from the Co_3O_4 support, especially during the initial 400 h (Fig. S14), which should be responsible for the slightly increased OER overpotentials (ΔE = 52 mV, Fig. 3e) during the chronopotentiometric measurements. Notably, the very slow dissolution of Ir species (Fig. S14) and the well-maintained XRD patterns (Fig. S15) suggest excellent OER stability. More encouragingly, the S-number (a metric for electrocatalyst stability)[53] reaches 5.6 × 10^5 at 10 mA cm^{-2} for the IrO_2/Co_3O_4 electrode, standing among the highest level reported for Ir-based electrocatalysts (Fig. S16 and Table S5). All these electrochemical results are evidence for the excellent activity and stability of IrO_2/Co_3O_4 for long-term OER under acidic conditions, exceeding those of most reported electrocatalysts where Ir species are dispersed on Co-based oxides (Fig. 3f and Table S4), which should be attributed to SMOSI, regulating OER intermediate behavior and thus reaction pathways.

As inferred from the above analytical results, the OER overpotential required by IrO_2/Co_3O_4 at a current density of 10 mA cm^{-2} (256 mV) is significantly lower than the theoretical minimum overpotential (370 ± 100 mV) limited by the scaling relationship, indicating that the reaction pathway for OER over IrO_2/Co_3O_4 should be different from the conventional adsorbate evolution mechanism (AEM). With the lattice-oxygen-mediated mechanism (LOM) excluded by using tetramethylammonium cation (TMA^+) as a chemical probe (Fig. S17),[54] the pH-dependent activity was evaluated and plotted to further deepen insights into the reaction pathway taking place at the obtained IrO_2/Co_3O_4 electrode. At a potential of 1.55 V *vs.* RHE, the very slight change in the logarithm of OER current densities dependent on pH values with a slope of −0.14 (Fig. 4a and Fig. S18a), suggests that commercial IrO_2 should drive OER by following the conventional AEM with a concerted proton–electron transfer (CPET) process.[55] In comparison, the IrO_2/Co_3O_4 electrode exhibits more significant dependence on pH values with a slope of −0.81 for OER activity (Fig. 4a and Fig. S18b), implying a nonconcerted proton–electron transfer (nCPET) process. It has

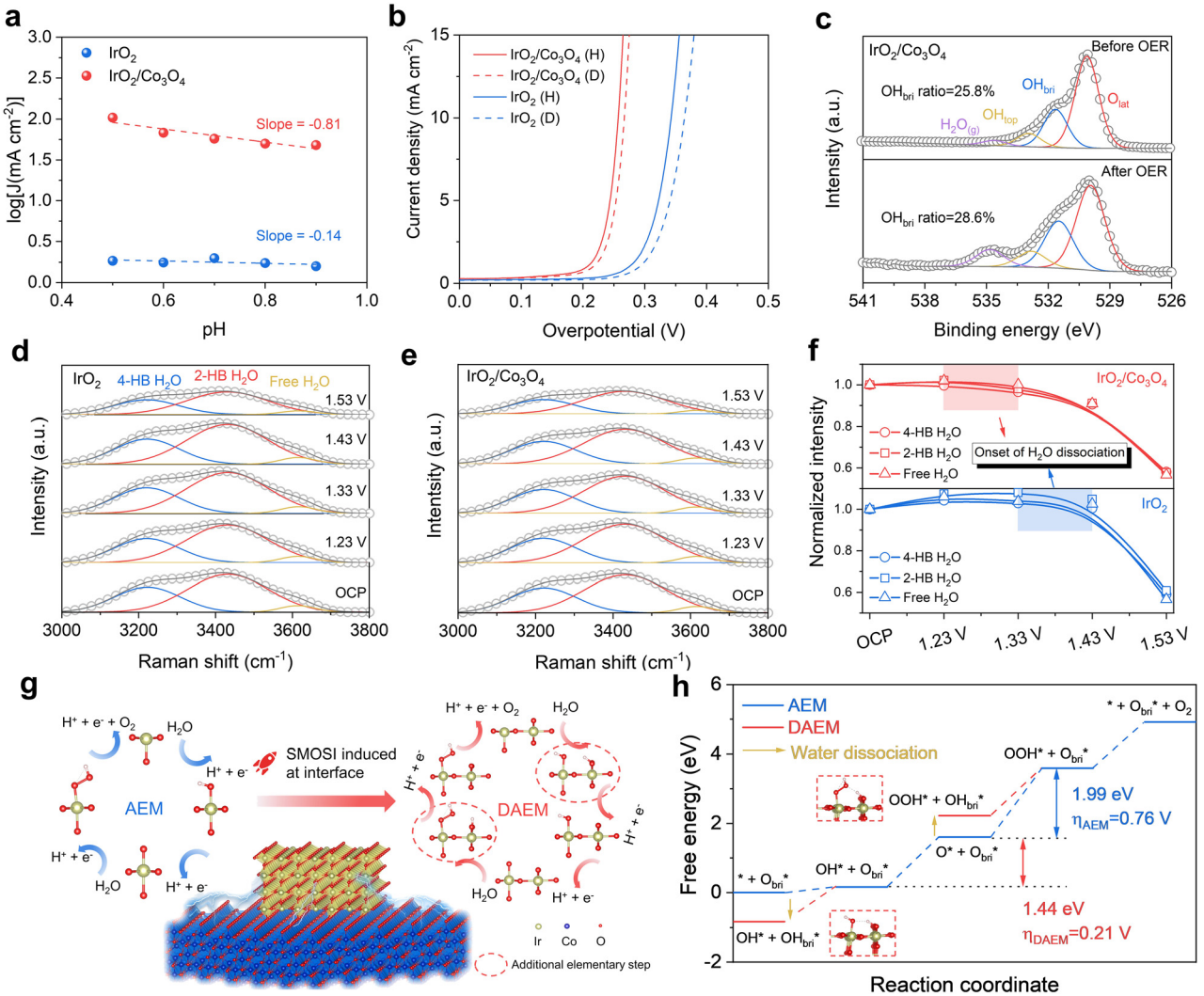

Fig. 4 (a) pH-Dependent curves plotted logarithmically for OER current densities recorded for IrO_2 and IrO_2/Co_3O_4 at 1.55 V *vs.* RHE at different pH values. (b) LSV curves of IrO_2 and IrO_2/Co_3O_4 measured in proton (0.5 M H_2SO_4 in H_2O) and deuterium (0.5 M H_2SO_4 in D_2O) electrolytes. (c) O 1s XPS spectra of IrO_2/Co_3O_4 before and after measuring OER at 200 mA cm^{-2} for 24 hours. *In situ* Raman spectra of interfacial water on the (d) IrO_2 and (e) IrO_2/Co_3O_4 electrodes collected at different applied potentials, from OCP to 1.53 V *vs.* RHE. (f) Potential-dependent normalized signal intensity of 4-HB H_2O, 2-HB H_2O and free H_2O collected from *in situ* Raman spectra, with normalization based on the Raman spectra collected at OCP. (g) Schematic illustration of AEM and DAEM for OER over IrO_2/Co_3O_4. (h) Calculated Gibbs free energy diagrams for OER over IrO_2/Co_3O_4 by following AEM and DAEM.

been well documented that the nCPET process should be beneficial to electrocatalytic OER activity, accompanied by a deprotonation process with decoupled electron transfer.[37] To investigate the deprotonation process taking place in OER over the IrO_2/Co_3O_4 electrode, kinetic isotope effect (KIE) measurements were conducted in proton (0.5 M H_2SO_4 in H_2O) and deuterium (0.5 M H_2SO_4 in D_2O) electrolytes, through Tafel analysis obtained from LSV plots (Fig. 4b and Fig. S19).[56] The KIE value was determined from the ratio of rate constants collected in proton (k_H) and deuterium (k_D) electrolytes (Fig. S19). Given the much larger mass of the D atom than of the H atom, replacing H_2O with D_2O would impede the kinetics of pathways involving protons during OER in aqueous solution, with a KIE value larger than 1 ($k_H > k_D$). Therefore, the KIE value can serve as a direct indicator for proton transfer being involved in the rate-determining step (RDS) for OER.[35,37,42] At low current density (less than 15 mA cm^{-2}), the KIE value (k_H/k_D) based on Tafel analysis is calculated to be 1.59 for IrO_2/Co_3O_4 (Fig. S19), much smaller than for IrO_2 (1.67). This significantly decreased KIE value is good evidence for the accelerated proton transfer process for IrO_2/Co_3O_4, with SMOSI induced at interfaces benefitting the deprotonation process. Moreover, for both IrO_2 and IrO_2/Co_3O_4, the KIE values in the OER potential regions surpass the upper limit of secondary KIE (~1.5), indicating that proton transfer should be involved in the rate-determining step (RDS) for acidic OER.[57] Such proton transfer relies on the oxygen species, as well explained by the O 1s XPS spectra. One could observe four distinct signals at *ca.* 530.1, 531.5, 533.0, and 534.0–535.0 eV, for IrO_2/Co_3O_4 (Fig. 4c), which should be assigned to lattice oxygen (O_{lat}),

protonated bridging oxygen (OH_{bri}), adsorbed hydroxyl (OH_{ads}) at unsaturated Ir sites, and the gas phase of water molecules ($H_2O_{(g)}$), respectively.[34] Notably, the ratio of OH_{bri} in O 1s XPS remains almost unchanged for Co_3O_4 and IrO_2 before and after OER (Fig. S20), while IrO_2/Co_3O_4 reveals an obvious increase in the OH_{bri} signal intensity after OER (Fig. 4c). Given that water dissociation happened mainly at the active sites, this enhanced OH_{bri} signal intensity should be attributed to the highly dispersed IrO_2 nanoparticles on the IrO_2/Co_3O_4 electrode during OER, as already evidenced by SEM-EDS (Fig. S13) and XPS analyses (Table S2).

It could thus be reasonably deduced that the bridging oxygen (O_{bri}, Fig. S21) sites in the IrO_2 nanoparticles anchored on the Co_3O_4 support should serve as proton acceptors to generate OH_{bri} intermediates, thereby accelerating the deprotonation process for OER. All the above electrochemical and spectral analyses could together claim that the deprotonation process in acidic OER could be accelerated over the IrO_2/Co_3O_4 electrode with SMOSI benefitting the O_{bri} sites to promote proton transfer and thus improve OER electrocatalysis.

Interfacial water as the proton source in acidic OER was monitored by *in situ* Raman spectra to further unravel the underlying mechanism of the accelerated deprotonation process during OER over IrO_2/Co_3O_4. Both IrO_2 and IrO_2/Co_3O_4 show a broad band at 3000–3800 cm^{-1}, related to the O–H stretching mode of interfacial water, which could be further fitted into three signals at *ca.* 3320, 3435 and 3620 cm^{-1} (Fig. 4d and e), corresponding to 4-coordinated hydrogen-bonded water (4-HB H_2O), 2-coordinated hydrogen-bonded water (2-HB H_2O) and free water (Free H_2O) (Fig. S22), respectively.[58,59] With normalization based on Raman spectra collected at open circuit potential (OCP), one should note that these signals assigned to interfacial water are gradually decreased, depending on the increased applied potentials (Fig. 4f), revealing the dissociation of interfacial water along with the supply of H and O atoms for OER. Furthermore, the onset of water dissociation, defined as the potential region in which the normalized signal intensity starts to decrease, is lower for IrO_2/Co_3O_4 (at 1.23–1.33 V *vs.* RHE) than for IrO_2 (at 1.33–1.43 V *vs.* RHE), suggesting that water dissociation could be facilitated over the IrO_2/Co_3O_4 electrode, as induced by the accelerated deprotonation process. This facilitated water dissociation could be verified by the much lowered kinetic energy barrier at the O_{bri} sites calculated for IrO_2/Co_3O_4 relative to IrO_2 (Fig. S23). To understand water dissociation at the level of electronic structure, the projected densities of states (PDOS) of O_{bri} sites in IrO_2 and IrO_2/Co_3O_4 were further investigated (Fig. S24). It is clear that IrO_2/Co_3O_4 exhibits an obvious upshift in the O_{bri} p-band centers (E_p) of −2.41 eV compared to IrO_2 (−2.66 eV), as supported by the elongated Ir–O bonds in IrO_2/Co_3O_4 (Fig. 2e). Such an upshift in E_p indicates that SMOSI could cause less filling of antibonding states of O_{bri} for stronger acceptance of protons in IrO_2/Co_3O_4, facilitating the formation of OH_{bri} intermediates during water dissociation. These experimental results and theoretical calculations disclose that water dissociation could be accelerated for efficient acidic OER over the IrO_2/Co_3O_4 electrode *via* SMOSI, steering the behavior of intermediates and the reaction pathway.

Inspired by the above analysis, a deprotonation-assisted adsorbate evolution mechanism (DAEM) could be proposed for acidic OER over the IrO_2/Co_3O_4 electrode to rationalize the excellent OER activity by breaking the scaling relationship in a conventional AEM. This proposed DAEM involves water dissociation at O_{bri} sites, along with the formation of OH_{bri} intermediates through an nCPET process (Fig. 4g), as supported by the pH-dependent OER activity (Fig. 4a). With additional elementary steps involved in DAEM through the nCPET process for the generation of OH* and OOH* intermediates, the scaling relationship in a conventional AEM could be broken, contributing to a reduced energy barrier for the RDS for greatly enhanced OER activity. To confirm the above insights, the Gibbs free energy changes were then calculated for IrO_2/Co_3O_4 with OER taking place *via* a conventional AEM and the proposed DAEM (Fig. 4h). It is observable that the RDS transforms from the generation of OOH* intermediates (O* → OOH*) for conventional AEM to the generation of O* intermediates (OH* → O*) for the proposed DAEM on IrO_2/Co_3O_4, with the calculated OER overpotential decreasing from 0.76 to 0.21 V. For the RDS taking place on IrO_2/Co_3O_4 by following DAEM, the OH* intermediates would convert into O* intermediates *via* the cleavage of O–H bonds, agreeing well with proton transfer participating in the RDS, as revealed by the KIE value (Fig. S19). Compared to IrO_2 following a conventional AEM (Fig. S25), IrO_2/Co_3O_4 drives acidic OER *via* the DAEM with the calculated overpotential much decreased and even exceeding the top of the OER volcano plot (Fig. S26). From these theoretical analyses, it can be concluded that the SMOSI induced at the IrO_2/Co_3O_4 interface could increase the E_p of O_{bri} sites with the strengthened acceptance of protons for accelerating water dissociation at O_{bri} sites. Consequently, a DAEM could be reasonably proposed and anticipated for the excellent performance for acidic OER over IrO_2/Co_3O_4, by breaking the scaling relationship associated with the conventional AEM (370 ± 100 mV).

To evaluate the application potential of the IrO_2/Co_3O_4 electrode for water splitting at an industrial level, a proton exchange membrane water electrolyzer (PEMWE) was assembled with IrO_2/Co_3O_4 as the anode and Pt/C as the cathode for water electrolysis (Fig. 5a). The recorded polarization curves (Fig. 5b) show cell voltages of 1.64 and 1.77 V required by the IrO_2/Co_3O_4||Pt/C PEMWE to achieve current densities of 0.5 and 1 A cm^{-2}, respectively, much lower than those of the IrO_2||Pt/C PEMWE (1.95 V at 0.5 A cm^{-2} and 2.18 V at 1 A cm^{-2}). This significant enhancement in OER performance realized over the IrO_2/Co_3O_4||Pt/C PEMWE could be further proved from the fitted EIS plots (Fig. 5c and Fig. S27), with charge transfer resistance greatly decreased from 4.04 Ω cm^2 for the IrO_2||Pt/C PEMWE to 0.22 Ω cm^2 for the IrO_2/Co_3O_4||Pt/C PEMWE, indicating improved kinetics for water electrolysis. The overvoltage, which could be divided into kinetic overvoltage, ohmic overvoltage and mass-transfer overvoltage, was then analyzed to investigate the origin of the excellent water electrolysis activity

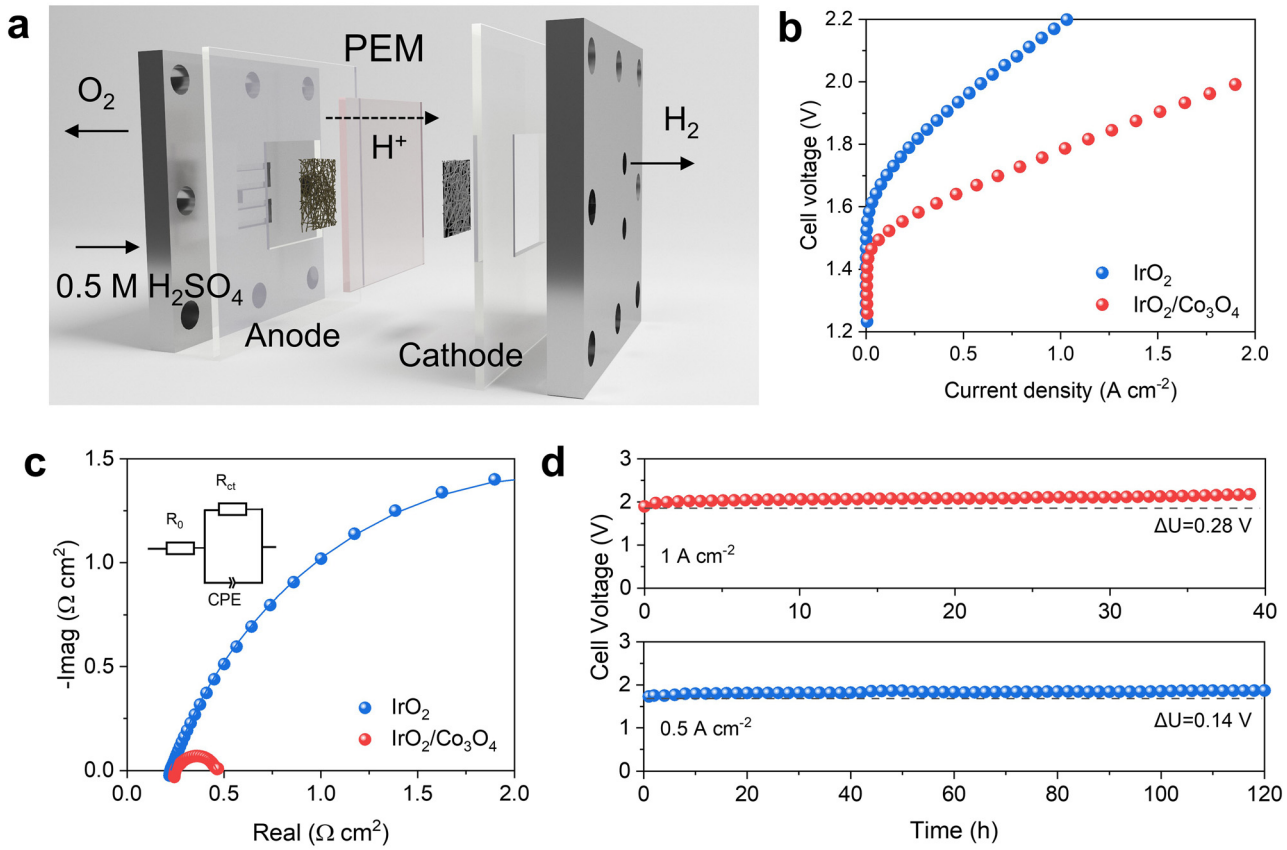

Fig. 5 (a) Schematic illustration of a PEMWE. (b) Polarization curves of a PEMWE assembled with IrO_2/Co_3O_4 or commercial IrO_2 as the anode and Pt/C as the cathode. (c) EIS plots recorded at a cell voltage of 1.5 V. (d) Stability test of the assembled IrO_2/Co_3O_4||Pt/C PEMWE operated at current densities of 1 and 0.5 A cm^{-2}.

for the IrO_2/Co_3O_4||Pt/C PEMWE (Fig. S28).[60] It should be noted that the kinetic overvoltage and mass-transfer overvoltage are much lower in the IrO_2/Co_3O_4||Pt/C PEMWE than in the IrO_2||Pt/C PEMWE at a current density of 1 A cm^{-2}, suggesting favorable reaction kinetics and fast mass transport. Such improvements can be attributed to the enhanced intrinsic OER activity and self-supported particulate structure of the IrO_2/Co_3O_4 electrode, which are key factors for a high-performance PEMWE. Chronoamperometric tests show that the IrO_2/Co_3O_4||Pt/C PEMWE could be stably operated at current densities of 0.5 and 1 A cm^{-2} for at least 120 and 40 h (Fig. 5d), respectively. Encouragingly, benefiting from SMOSI-accelerated deprotonation, the PEMWE with an IrO_2/Co_3O_4 electrode of low-density Ir loading achieves remarkable performance, comparable to previously reported results (Table S6). All the above electrochemical results demonstrate that the IrO_2/Co_3O_4 electrode could serve as a promising anode in a PEMWE, with both excellent activity and stability realized for water electrolysis at an industrial level.

3. Conclusion

In summary, ultrasmall IrO_2 nanoparticles were firmly anchored on an acid-resistant Co_3O_4 support through galvanic replacement, with a low overpotential of 256 mV at 10 mA cm^{-2} achieved over the obtained IrO_2/Co_3O_4 electrode for acidic OER and long-term stability exceeding 1000 h. Encouragingly, a PEMWE assembled with IrO_2/Co_3O_4 as the anode and Pt/C as the cathode could survive 120 h and 40 h of operation at industrial-level current densities of 0.5 and 1 A cm^{-2}, with cell voltages of 1.64 and 1.77 V, respectively. It was experimentally and theoretically revealed that the SMOSI induced at the lattice-mismatched IrO_2/Co_3O_4 interfaces increases the p-band centers of O_{bri} sites in the Ir–O_{bri} bonds. Such increased p-band centers strengthen proton acceptance at O_{bri} sites, accelerating the deprotonation process. Consequently, a DAEM could be reasonably proposed to elucidate the excellent performance for acidic OER over IrO_2/Co_3O_4, by breaking the scaling relationship in a conventional AEM (370 ± 100 mV). This study demonstrates a promising approach for regulating the deprotonation process on O_{bri} sites *via* SMOSI for efficient and stable acidic OER, and also inspires the design of applicable and low-noble-metal electrocatalysts for an industrial-level PEMWE.

Author contributions

All authors contributed to the collection and discussion of the content. All authors helped to revise the manuscript before submission.

Conflicts of interest

There are no conflicts to declare.

Data availability

The data supporting this article have been included as part of the supplementary information (SI). Supplementary information: Experimental section (material synthesis, characterizations, and DFT calculations), SEM, SEM-EDS, ICP-MS, XRD, EXAFS, electrocatalytic measurements, and their related discussions. See DOI: https://doi.org/10.1039/d5mh01620g.

Acknowledgements

The authors thank the financial support from the National Natural Science Foundation of China (Grant No. 52488201, 52225606), the Key R&D Program of Shaanxi Province (No. 2024CY-GJHX-28), the CNPC Innovation Fund (2022DQ02-0603), the ''Fundamental Research Funds for the Central Universities''.

Notes and references

1 J. A. Turner, *Science*, 2004, **305**, 972–974.
2 I. Staffell, D. Scamman, A. Velazquez Abad, P. Balcombe, P. E. Dodds, P. Ekins, N. Shah and K. R. Ward, *Energy Environ. Sci.*, 2019, **12**, 463–491.
3 D. Zhao, Y. Wang, C.-L. Dong, Y.-C. Huang, J. Chen, F. Xue, S. Shen and L. Guo, *Nat. Energy*, 2021, **6**, 388–397.
4 H. Deng, C.-L. Dong, Y.-C. Huang, M. Wang, Z. Yu, Y. Wang, H. Li, J. Chen and S. Shen, *ACS Mater. Lett.*, 2024, **6**, 3272–3281.
5 L. Chong, G. Gao, J. Wen, H. Li, H. Xu, Z. Green, J. D. Sugar, A. J. Kropf, W. Xu, X.-M. Lin, H. Xu, L.-W. Wang and D.-J. Liu, *Science*, 2023, **380**, 609–616.
6 Z. W. Seh, J. Kibsgaard, C. F. Dickens, I. Chorkendorff, J. K. Nørskov and T. F. Jaramillo, *Science*, 2017, **355**, eaad4998.
7 H. Liu, Z. Zhang, J. Fang, M. Li, M. G. Sendeku, X. Wang, H. Wu, Y. Li, J. Ge, Z. Zhuang, D. Zhou, Y. Kuang and X. Sun, *Joule*, 2023, **7**, 558–573.
8 Q. Wang, Y. Cheng, H. B. Tao, Y. Liu, X. Ma, D.-S. Li, H. B. Yang and B. Liu, *Angew. Chem., Int. Ed.*, 2023, **62**, e202216645.
9 R.-T. Liu, Z.-L. Xu, F.-M. Li, F.-Y. Chen, J.-Y. Yu, Y. Yan, Y. Chen and B. Y. Xia, *Chem. Soc. Rev.*, 2023, **52**, 5652–5683.
10 L. Li, G. Zhang, C. Zhou, F. Lv, Y. Tan, Y. Han, H. Luo, D. Wang, Y. Liu, C. Shang, L. Zeng, Q. Huang, R. Zeng, N. Ye, M. Luo and S. Guo, *Nat. Commun.*, 2024, **15**, 4974.
11 S. Ge, R. Xie, B. Huang, Z. Zhang, H. Liu, X. Kang, S. Hu, S. Li, Y. Luo, Q. Yu, J. Wang, G. Chai, L. Guan, H.-M. Cheng and B. Liu, *Energy Environ. Sci.*, 2023, **16**, 3734–3742.
12 H. Gao, Z. Xiao, S. Du, T. Liu, Y.-C. Huang, J. Shi, Y. Zhu, G. Huang, B. Zhou, Y. He, C.-L. Dong, Y. Li, R. Chen and S. Wang, *Angew. Chem., Int. Ed.*, 2023, **62**, e202313954.
13 F.-Y. Chen, Z.-Y. Wu, Z. Adler and H. Wang, *Joule*, 2021, **5**, 1704–1731.
14 A. Li, S. Kong, K. Adachi, H. Ooka, K. Fushimi, Q. Jiang, H. Ofuchi, S. Hamamoto, M. Oura, K. Higashi, T. Kaneko, T. Uruga, N. Kawamura, D. Hashizume and R. Nakamura, *Science*, 2024, **384**, 666–670.
15 J. Xu, H. Jin, T. Lu, J. Li, Y. Liu, K. Davey, Y. Zheng and S.-Z. Qiao, *Sci. Adv.*, 2023, **9**, eadh1718.
16 Y. Weng, K. Wang, S. Li, Y. Wang, L. Lei, L. Zhuang and Z. Xu, *Adv. Sci.*, 2023, **10**, 2205920.
17 Z. Shi, J. Li, J. Jiang, Y. Wang, X. Wang, Y. Li, L. Yang, Y. Chu, J. Bai, J. Yang, J. Ni, Y. Wang, L. Zhang, Z. Jiang, C. Liu, J. Ge and W. Xing, *Angew. Chem., Int. Ed.*, 2022, **61**, e202212341.
18 Y. Wang, M. Zhang, Z. Kang, L. Shi, Y. Shen, B. Tian, Y. Zou, H. Chen and X. Zou, *Nat. Commun.*, 2023, **14**, 5119.
19 C. Yang, W. Ling, Y. Zhu, Y. Yang, S. Dong, C. Wu, Z. Wang, S. Yang, J. Li, G. Wang, Y. Huang, B. Yang, Q. Cheng, Z. Liu and H. Yang, *Appl. Catal., B*, 2024, **358**, 124462.
20 S. Pichaikaran, S. Kotteswaran, M. K. Francis, P. B. Bhargav, W. Bo, N. Ahmed and B. C, *Mol. Catal.*, 2023, **547**, 113383.
21 W. Q. Zaman, W. Sun, Z.-H. Zhou, Y. Wu, L. Cao and J. Yang, *ACS Appl. Energy Mater.*, 2018, **1**, 6374–6380.
22 Y. Zhu, J. Wang, T. Koketsu, M. Kroschel, J.-M. Chen, S.-Y. Hsu, G. Henkelman, Z. Hu, P. Strasser and J. Ma, *Nat. Commun.*, 2022, **13**, 7754.
23 G. Li, A. Priyadarsini, Z. Xie, S. Kang, Y. Liu, X. Chen, S. Kattel and J. G. Chen, *J. Am. Chem. Soc.*, 2025, **147**, 7008–7016.
24 J. Shan, C. Ye, S. Chen, T. Sun, Y. Jiao, L. Liu, C. Zhu, L. Song, Y. Han, M. Jaroniec, Y. Zhu, Y. Zheng and S.-Z. Qiao, *J. Am. Chem. Soc.*, 2021, **143**, 5201–5211.
25 Y. Liu, Y. Chen, X. Mu, Z. Wu, X. Jin, J. Li, Y. Xu, L. Yang, X. Xi, H. Jang, Z. Lei, Q. Liu, S. Jiao, P. Yan, X. Li and R. Cao, *ACS Catal.*, 2023, **13**, 3757–3767.
26 K. Hua, X. Li, Z. Rui, X. Duan, Y. Wu, D. Yang, J. Li and J. Liu, *ACS Catal.*, 2024, **14**, 3712–3724.
27 J. Rossmeisl, Z. W. Qu, H. Zhu, G. J. Kroes and J. K. Nørskov, *J. Electroanal. Chem.*, 2007, **607**, 83–89.
28 I. C. Man, H.-Y. Su, F. Calle-Vallejo, H. A. Hansen, J. I. Martínez, N. G. Inoglu, J. Kitchin, T. F. Jaramillo, J. K. Nørskov and J. Rossmeisl, *ChemCatChem*, 2011, **3**, 1159–1165.
29 J. Song, C. Wei, Z.-F. Huang, C. Liu, L. Zeng, X. Wang and Z. J. Xu, *Chem. Soc. Rev.*, 2020, **49**, 2196–2214.
30 Z.-F. Huang, J. Song, S. Dou, X. Li, J. Wang and X. Wang, *Matter*, 2019, **1**, 1494–1518.
31 Z.-F. Huang, J. Song, Y. Du, S. Xi, S. Dou, J. M. V. Nsanzimana, C. Wang, Z. J. Xu and X. Wang, *Nat. Energy*, 2019, **4**, 329–338.
32 Z. Shi, J. Li, Y. Wang, S. Liu, J. Zhu, J. Yang, X. Wang, J. Ni, Z. Jiang, L. Zhang, Y. Wang, C. Liu, W. Xing and J. Ge, *Nat. Commun.*, 2023, **14**, 843.
33 A. Grimaud, A. Demortière, M. Saubanère, W. Dachraoui, M. Duchamp, M.-L. Doublet and J.-M. Tarascon, *Nat. Energy*, 2016, **2**, 16189.

34 Y. Wen, C. Liu, R. Huang, H. Zhang, X. Li, F. P. García de Arquer, Z. Liu, Y. Li and B. Zhang, *Nat. Commun.*, 2022, **13**, 4871.
35 S. Chen, S. Zhang, L. Guo, L. Pan, C. Shi, X. Zhang, Z.-F. Huang, G. Yang and J.-J. Zou, *Nat. Commun.*, 2023, **14**, 4127.
36 H. Jia, Z. Liao, J. Zhu and W. Luo, *Renewables*, 2024, **2**, 204–212.
37 L. Deng, S.-F. Hung, S. Liu, S. Zhao, Z.-Y. Lin, C. Zhang, Y. Zhang, A.-Y. Wang, H.-Y. Chen, J. Peng, R. Ma, L. Jiao, F. Hu, L. Li and S. Peng, *J. Am. Chem. Soc.*, 2024, **146**, 23146–23157.
38 H. Wu, J. Chang, J. Yu, S. Wang, Z. Hu, G. I. N. Waterhouse, X. Yong, Z. Tang, J. Chang and S. Lu, *Nat. Commun.*, 2024, **15**, 10315.
39 Y. Wu, C. Guo, R. Yao, K. Zhang, J. Li and G. Liu, *Adv. Funct. Mater.*, 2024, **34**, 2410193.
40 L.-P. Yuan, W.-J. Jiang, X.-L. Liu, Y.-H. He, C. He, T. Tang, J. Zhang and J.-S. Hu, *ACS Catal.*, 2020, **10**, 13227–13235.
41 H. Cheng, C. Wang, D. Qin and Y. Xia, *Acc. Chem. Res.*, 2023, **56**, 900–909.
42 J. Huang, H. Sheng, R. D. Ross, J. Han, X. Wang, B. Song and S. Jin, *Nat. Commun.*, 2021, **12**, 3036.
43 H. Li, W. Wang, S. Xue, J. He, C. Liu, G. Gao, S. Di, S. Wang, J. Wang, Z. Yu and L. Li, *J. Am. Chem. Soc.*, 2024, **146**, 9124–9133.
44 K. Qi, X. Cui, L. Gu, S. Yu, X. Fan, M. Luo, S. Xu, N. Li, L. Zheng, Q. Zhang, J. Ma, Y. Gong, F. Lv, K. Wang, H. Huang, W. Zhang, S. Guo, W. Zheng and P. Liu, *Nat. Commun.*, 2019, **10**, 5231.
45 Z. Li, Q. Wang, X. Bai, M. Wang, Z. Yang, Y. Du, G. E. Sterbinsky, D. Wu, Z. Yang, H. Tian, F. Pan, M. Gu, Y. Liu, Z. Feng and Y. Yang, *Energy Environ. Sci.*, 2021, **14**, 5035–5043.
46 K. Lee, J. Shim, H. Ji, J. Kim, H. S. Lee, H. Shin, M. S. Bootharaju, K.-S. Lee, W. Ko, J. Lee, K. Kim, S. Yoo, S. Heo, J. Ryu, S. Back, B.-H. Lee, Y.-E. Sung and T. Hyeon, *Energy Environ. Sci.*, 2024, **17**, 3618–3628.
47 Y. Chen, H. Li, J. Wang, Y. Du, S. Xi, Y. Sun, M. Sherburne, J. W. Ager, A. C. Fisher and Z. J. Xu, *Nat. Commun.*, 2019, **10**, 572.
48 F. Liao, K. Yin, Y. Ji, W. Zhu, Z. Fan, Y. Li, J. Zhong, M. Shao, Z. Kang and Q. Shao, *Nat. Commun.*, 2023, **14**, 1248.
49 Z. Shi, Y. Wang, J. Li, X. Wang, Y. Wang, Y. Li, W. Xu, Z. Jiang, C. Liu, W. Xing and J. Ge, *Joule*, 2021, **5**, 2164–2176.
50 W. H. Lee, H. N. Nong, C. H. Choi, K. H. Chae, Y. J. Hwang, B. K. Min, P. Strasser and H.-S. Oh, *Appl. Catal., B*, 2020, **269**, 118820.
51 L. Zhang, Y. Lei, Y. Yang, D. Wang, Y. Zhao, X. Xiang, H. Shang and B. Zhang, *Adv. Sci.*, 2024, **11**, 2407475.
52 J. Wang, C.-S. Hsu, T.-S. Wu, T.-S. Chan, N.-T. Suen, J.-F. Lee and H. M. Chen, *Nat. Commun.*, 2023, **14**, 6576.
53 S. Geiger, O. Kasian, M. Ledendecker, E. Pizzutilo, A. M. Mingers, W. T. Fu, O. Diaz-Morales, Z. Li, T. Oellers, L. Fruchter, A. Ludwig, K. J. J. Mayrhofer, M. T. M. Koper and S. Cherevko, *Nat. Catal.*, 2018, **1**, 508–515.
54 N. Yao, H. Jia, J. Zhu, Z. Shi, H. Cong, J. Ge and W. Luo, *Chem*, 2023, **9**, 1882–1896.
55 L. Giordano, B. Han, M. Risch, W. T. Hong, R. R. Rao, K. A. Stoerzinger and Y. Shao-Horn, *Catal. Today*, 2016, **262**, 2–10.
56 E. C. M. Tse, T. T. H. Hoang, J. A. Varnell and A. A. Gewirth, *ACS Catal.*, 2016, **6**, 5706–5714.
57 W. Li, F. Li, H. Yang, X. Wu, P. Zhang, Y. Shan and L. Sun, *Nat. Commun.*, 2019, **10**, 5074.
58 Y.-H. Wang, S. Zheng, W.-M. Yang, R.-Y. Zhou, Q.-F. He, P. Radjenovic, J.-C. Dong, S. Li, J. Zheng, Z.-L. Yang, G. Attard, F. Pan, Z.-Q. Tian and J.-F. Li, *Nature*, 2021, **600**, 81–85.
59 S. Zhu, R. Yang, H. J. W. Li, S. Huang, H. Wang, Y. Liu, H. Li and T. Zhai, *Angew. Chem., Int. Ed.*, 2024, **63**, e202319462.
60 L. Tao, F. Lv, D. Wang, H. Luo, F. Lin, H. Gong, H. Mi, S. Wang, Q. Zhang, L. Gu, M. Luo and S. Guo, *Joule*, 2024, **8**, 450–460.

